



# AMERICAN METEOROLOGICAL SOCIETY

*Journal of Climate*

## **EARLY ONLINE RELEASE**

This is a preliminary PDF of the author-produced manuscript that has been peer-reviewed and accepted for publication. Since it is being posted so soon after acceptance, it has not yet been copyedited, formatted, or processed by AMS Publications. This preliminary version of the manuscript may be downloaded, distributed, and cited, but please be aware that there will be visual differences and possibly some content differences between this version and the final published version.

The DOI for this manuscript is doi: 10.1175/JCLI-D-11-00268.1

The final published version of this manuscript will replace the preliminary version at the above DOI once it is available.

If you would like to cite this EOR in a separate work, please use the following full citation:

Webber, B., D. Stevens, A. Matthews, and K. Heywood, 2011: Dynamical ocean forcing of the Madden-Julian Oscillation at lead times of up to five months. *J. Climate*. doi:10.1175/JCLI-D-11-00268.1, in press.



# Dynamical ocean forcing of the Madden-Julian Oscillation at lead times of up to five months

BENJAMIN G. M. WEBBER<sup>1</sup> \*, DAVID P. STEVENS<sup>2</sup>, ADRIAN J. MATTHEWS<sup>1,2</sup>  
AND KAREN J. HEYWOOD<sup>1</sup>

*1 School of Environmental Sciences, University of East Anglia, Norwich, United Kingdom*

*2 School of Mathematics, University of East Anglia, Norwich, United Kingdom*

---

\* *Corresponding author address:* Benjamin Webber, School of Environmental Sciences, University of East Anglia, Norwich Research Park, Norwich, NR4 7TJ.

E-mail: b.webber@uea.ac.uk

## ABSTRACT

We show that a simple three-dimensional ocean model linearised about a resting basic state can accurately simulate the dynamical ocean response to wind forcing by the Madden-Julian Oscillation (MJO). This includes the propagation of equatorial waves in the Indian Ocean, from the generation of oceanic equatorial Kelvin waves to the arrival of downwelling oceanic equatorial Rossby waves in the western Indian Ocean, where they have been shown to trigger MJO convective activity. Simulations with idealised wind forcing suggest that the latitudinal width of this forcing plays a crucial role in determining the potential for such feedbacks. Forcing the model with composite MJO winds accurately captures the global ocean response, demonstrating that the observed ocean dynamical response to the MJO can be interpreted as a linear response to surface wind forcing.

The model is then applied to study “primary” Madden-Julian events, which are not immediately preceded by any MJO activity nor by any apparent atmospheric triggers, but have been shown to coincide with the arrival of downwelling oceanic equatorial Rossby waves. Case study simulations show how this oceanic equatorial Rossby wave activity is partly forced by reflection of an oceanic equatorial Kelvin wave triggered by a westerly wind burst 140 days previously, and partly directly forced by easterly wind stress anomalies around 40 days prior to the event. This suggests predictability for primary Madden-Julian events on times scales of up to five months, following the re-emergence of oceanic anomalies forced by winds almost half a year earlier.

# 1. Introduction

The dynamics of the equatorial oceans are dominated by equatorial Kelvin and Rossby waves, on time scales from intraseasonal (Kessler et al. 1995; Hendon et al. 1998) to interannual (Battisti 1988; McPhaden 1999). These are planetary scale internal waves with wavelengths of thousands of km that affect sea surface height (SSH) and pycnocline depth. Variations in pycnocline depth are several orders of magnitude larger than the SSH anomalies and have the opposite sign; thus positive SSH anomalies correspond to a deeper mixed layer depth (MLD) and downwelling anomalies. This variability modifies the upper-ocean heat content and the mixing of cold subsurface waters, leading to changes in sea surface temperature (SST; McCreary 1983; Battisti 1988). These SST anomalies subsequently modulate atmospheric convection; such processes have been shown to be important for the El Niño-Southern Oscillation (ENSO; Battisti 1988; Kessler and McPhaden 1995; McPhaden 1999) and the Madden-Julian Oscillation (MJO; Han et al. 2001; Webber et al. 2010).

Equatorial Kelvin waves exhibit a single equatorial SSH maximum while equatorial Rossby waves have more complex meridional structures, the simplest and most commonly observed being the first meridional mode with symmetric off-equatorial SSH maxima (Chelton et al. 2003). A westerly wind burst on the equator will generate Ekman convergence, thus forcing a positive SSH anomaly on the equator, along with downwelling anomalies and an eastward current. These anomalies propagate along the equator as a downwelling Kelvin wave (Giese and Harrison 1990). Westerly wind bursts will typically also trigger upwelling Rossby waves due to off-equatorial Ekman divergence, although this is somewhat dependent on the meridional structure of the wind stress (Chelton et al. 2003).

For a continuously stratified ocean there are an infinite number of vertical (baroclinic) modes for both equatorial waves, in addition to the barotropic mode (sometimes referred to as the zeroth baroclinic mode). However, typically only the barotropic and first few baroclinic modes are observed to be important (Giese and Harrison 1990; Chelton and Schlax 1996; Wunsch 1997). The propagation speed of such waves depends upon both the baroclinic

mode and the stratification of the fluid through which they propagate. Equatorial Kelvin waves are nondispersive with the first baroclinic mode ( $n = 1$ ) phase speed  $c_e$  between around 2.4 and 3.0 m s<sup>-1</sup>, depending on the local stratification (Chelton et al. 1998). The first baroclinic mode equatorial Rossby wave phase speed,  $c$ , also depends on the meridional mode (Chelton et al. 2003), and follows the dispersion relation

$$c = \frac{-\beta}{k^2 + (2m + 1)\beta/c_e},$$

where  $\beta \approx 2.3 \times 10^{-11}$  m<sup>-1</sup> s<sup>-1</sup> is the meridional gradient of planetary vorticity,  $k$  is the zonal wavenumber, and  $m$  is the meridional mode number. Thus, long first baroclinic, first meridional, mode Rossby waves propagate westward at approximately  $\frac{c_e}{3}$  or around 0.8–1.0 m s<sup>-1</sup> in the Indian Ocean.

Kelvin waves can also propagate along coastal waveguides, with the coastline to the right (left) of the wave in the northern (southern) hemisphere. Coastal Kelvin waves can be generated by local wind stress forcing or by equatorial waves incident on a meridionally-oriented coastal boundary. However, the effect of sloping coastal bathymetry is to produce a coastally trapped wave which combines the properties of Kelvin waves and barotropic shelf waves, with modified phase speed and increased dispersion (Huthnance 1975; Brink 1982, 1991).

The Madden-Julian Oscillation (MJO) is the dominant atmospheric mode of intraseasonal variability in the tropics (Madden and Julian 1971, 1972). It is associated with convective, rainfall and wind variability with a periodicity of around 30–60 days, although it is only quasi-periodic and thus has a broadband spectral signal extending as far as 100 days (Salby and Hendon 1994). See Zhang (2005) and Lau and Waliser (2005) for a full review of the MJO and its impacts.

The MJO is an important source of surface wind stress variability and thus generates substantial oceanic equatorial wave activity (Hendon et al. 1998; Han et al. 2001; Weber et al. 2010). Observations have linked the MJO-generated oceanic equatorial Kelvin waves to the triggering of ENSO events (McPhaden 1999). There is also growing evidence

of the potential for oceanic equatorial Rossby waves in the Indian Ocean to force variability in the MJO (Webber et al. 2010, 2011) and for feedbacks between the two (Han et al. 2001; Han 2005; Fu 2007).

The MJO is sporadic, with periods of cyclical activity (“successive” events) interspersed with intervals of relative quiescence. “Primary” Madden-Julian (MJ) events are those that are not preceded by any coherent MJO activity. Here, we follow Matthews (2008) by examining the subset of primary events that begin in the western Indian Ocean, which accounts for the largest portion of such events. Matthews (2008) found no triggers or precursors from the atmospheric dynamics or thermodynamic interaction with the ocean for such events. However, Webber et al. (2011) showed, through a combination of case studies and composite analysis, that these events do coincide with the arrival of a downwelling oceanic equatorial Rossby wave in the western Indian Ocean, implying that such waves could act as a trigger. They suggested that the associated warm SST anomalies act to destabilise the atmospheric boundary layer, thus priming the atmosphere for the large scale convection associated with an MJ event. The western Indian Ocean appears to be a favourable region for such forcing to occur, possibly due to the relatively shallow thermocline (Xie et al. 2002), higher rates of entrainment cooling (McCreary et al. 1993) and the relatively weak intraseasonal surface heat fluxes here.

This paper examines the dynamical response of the Indian Ocean to the MJO and its potential to couple to the MJO through simulations in a linearised ocean circulation model. A combination of model runs forced by both idealised and realistic surface wind stress forcing are used. The pathways and time scales of the wave propagation are examined using simple idealised wind patches and the effects of stratification, bathymetry and forcing scale are analysed. Model runs with composite forcing are compared with the observational results of Webber et al. (2010) to validate the model performance and investigate further the global dynamical ocean response. The model is then run with observed winds from the period prior to a case study primary event on 24 September 2004. Comparison with observations

from that case study allows the key atmospheric forcing events to be identified and their relative importance to be tested. Thus we identify the time scales that are important for this primary MJ event triggering mechanism.

## 2. Observational Data and Model Forcing

The surface wind stress data used in this study are calculated using daily global 10 m wind velocities  $\mathbf{v}$  from the European Centre for Medium-range Weather Forecasts (ECMWF) Era-Interim data set. For compositing relative to the MJO, the period of 1 January 1990 to 31 December 2008 is used. The wind stress  $\tau$  is then approximated using the standard bulk formula  $\tau = \rho C_D |\mathbf{v}| \mathbf{v}$ , with the air density  $\rho = 1.23 \text{ kg m}^{-3}$  and the drag coefficient  $C_D = 1.5 \times 10^{-3}$ . This is calculated separately for the zonal and meridional components of the wind field and then spatially interpolated using cubic splines onto the  $1/3^\circ$  grid used in the ocean model.

The SSH anomalies used in this study are from the merged TOPEX/Poseidon-Earth Remote Sensing (T/P-ERS) satellite altimetry product (Fu et al. 1994; Ducet et al. 2000; Le Traon et al. 2001). Weekly data on a  $0.25^\circ$  grid were obtained for the period from 14 October 1992 to 23 January 2008, and then interpolated to daily values using cubic splines. SST data from the Tropical Microwave Imaging (TMI) satellite (Kummerow et al. 2000; Gentemann et al. 2004) were extracted from 1 January 1998 to 17 December 2008. The data are available as daily fields of the 3-day running-mean SST at  $0.25^\circ$  resolution. Outgoing long-wave radiation (OLR) is used as a proxy for tropical deep convective precipitation. The OLR data for this study were obtained as  $2.5^\circ$  resolution gridded daily output from the optimally-interpolated Liebmann and Smith (1996) data set. For comparison with the subsurface variability in the model, we use density data from the ECCO-GODAE ocean state estimate (Estimating the Circulation and Climate of the Ocean-Global Ocean Data Assimilation Experiment; Wunsch and Heimbach 2007), which we treat as “observations” in

the same sense as an atmospheric reanalysis product.

To construct composites of observational fields for surface forcing or comparison with model output, we use the eight phases of the MJO as defined by the Wheeler-Hendon index (Wheeler and Hendon 2004). Phase 1 corresponds to minimum convection over the Maritime Continent and the initiation of active convective anomalies in the western Indian Ocean. These anomalies move eastwards in each successive phase; by phase 4 the positive convective anomalies overlie the Maritime Continent while the suppressed convection has propagated into the western Pacific. A new region of suppressed convection originates in the western Indian Ocean at phase 5; phases 5–8 are thus equivalent to phases 1–4 with anomalies of the opposite sign.

The linear trend, mean and first three harmonics of the annual cycle were removed pointwise from each data set to produce detrended anomaly fields, which were then bandpass-filtered using a 20-200 day Lanczos filter. The use of such a broadband filter is motivated by its ability to exclude low-frequency climate signals as well as high-frequency noise while better retaining the MJO signal and the distinction between individual MJ events than a narrower filter window (Matthews 2000). The filter uses 241 symmetric weights, meaning that 120 days of data are lost at each end of the data set. All data sets were further truncated so that an integer number of calendar years are retained, thus avoiding seasonal bias. To investigate the oceanic response to the MJO, composites are created separately for each MJO phase, using all days within that phase when the amplitude of the Wheeler-Hendon index exceeds an arbitrary threshold value of 1.5, along with counter-clockwise rotation in the Wheeler-Hendon phase space to ensure eastwards propagation. The threshold value was chosen to select the stronger MJO events (whose impact on the ocean should be stronger and more coherent), as opposed to the threshold value of 1 chosen by Wheeler and Hendon (2004).

### 3. Model Description and Setup

The ocean model used for this study is a linearised version of the general circulation model described by Webb (1996). A similar approach was used by Anderson et al. (1979) to study the transient response in the North Atlantic to a change in wind forcing. There are no mean currents and the mean vertical potential density stratification,  $\bar{\rho}(z)$ , is independent of horizontal position. The equations of motion are

$$\begin{aligned}\frac{\partial u}{\partial t} - fv &= -\frac{1}{\rho_0 a \cos \phi} \frac{\partial p}{\partial \lambda} + A_h \nabla^2 u + K_m \frac{\partial^2 u}{\partial z^2}, \\ \frac{\partial v}{\partial t} + fu &= -\frac{1}{\rho_0 a} \frac{\partial p}{\partial \phi} + A_h \nabla^2 v + K_m \frac{\partial^2 v}{\partial z^2}, \\ \frac{\partial p}{\partial z} &= -\rho g, \\ \frac{1}{a \cos \phi} \frac{\partial u}{\partial \lambda} + \frac{1}{a \cos \phi} \frac{\partial}{\partial \phi} (v \cos \phi) + \frac{\partial w}{\partial z} &= 0, \\ \frac{\partial \rho}{\partial t} + w \frac{\partial \bar{\rho}}{\partial z} &= K_h \frac{\partial^2 \rho}{\partial z^2},\end{aligned}$$

where

$$\nabla^2(\mu) = \frac{1}{a^2 \cos^2 \phi} \frac{\partial^2 \mu}{\partial \lambda^2} + \frac{1}{a^2 \cos \phi} \frac{\partial}{\partial \phi} \left( \frac{\partial \mu}{\partial \phi} \cos \phi \right).$$

The variables  $\phi$ ,  $\lambda$ ,  $z$ ,  $t$ ,  $u$ ,  $v$ ,  $w$ ,  $p$ ,  $\rho$ , represent latitude, longitude, depth (negative of), time, zonal velocity, meridional velocity, vertical velocity, pressure, and density anomaly, respectively. The radius of the Earth is  $a$ ,  $g$  is the acceleration due to gravity, and  $\rho_0$  is a reference potential density. The Coriolis parameter  $f = 2\Omega \sin \phi$  where  $\Omega$  is the speed of angular rotation of the Earth. The horizontal eddy viscosity is  $A_h = 10^3 \text{ m}^2 \text{ s}^{-1}$  and the vertical eddy viscosity,  $K_m$  and diffusivity,  $K_h$ , are both set to  $10^{-4} \text{ m}^2 \text{ s}^{-1}$ . At the ocean surface a wind stress  $(\tau_s^\lambda, \tau_s^\phi)$  is applied and related to the ocean velocities by

$$\rho_0 K_m \frac{\partial}{\partial z} (u, v) = (\tau_s^\lambda, \tau_s^\phi)$$

and no flux of density is prescribed.

The model is configured quasi-globally (the Arctic and the Nordic Seas north of 67° N are omitted), with a horizontal resolution of  $1/3^\circ \times 1/3^\circ$  and 40 uneven levels in the vertical that vary smoothly from 10 m thickness at the sea surface to 300 m thickness at depth. The mean vertical potential density profile,  $\bar{\rho}$ , is taken from the Indian Ocean, calculated from the World Ocean Database 2001 (Levitus et al. 2002) over 10°N–10°S, 60–90°E (Figure 1). The model can also be configured with only two density layers, where the upper 12 model layers are given the surface potential density ( $1022.1 \text{ kg m}^{-3}$ ) and the remaining 28 layers the deepest layer potential density ( $1027.8 \text{ kg m}^{-3}$ ). The bathymetry of the model is shown in Figure 2, along with key geographical regions for this study and the pathway for the Indonesian Throughflow (ITF).

## 4. Idealised westerly wind burst forcing experiments

### *a. Control run*

Several studies have shown the importance of westerly wind bursts (WWBs) in forcing equatorial oceanic Kelvin waves (Giese and Harrison 1990; McPhaden et al. 1992; Kessler et al. 1995). The MJO is a major source of relatively long-lived WWBs at the same spatial scale as the resulting Kelvin waves, and is thus an effective forcing mechanism (Hendon et al. 1998). Here we idealise this forcing mechanism by applying a Gaussian WWB centred on the equator ( $\phi_0 = 0$ ) at  $\lambda_0 = 75^\circ\text{E}$ , with a decay scale of  $10^\circ$  in both longitude ( $W_\lambda$ ) and latitude ( $W_\phi$ ). The wind forcing is applied constantly with a peak westerly magnitude of  $\tau_0 = 0.1 \text{ N m}^{-2}$  (corresponding to a windspeed of  $7.4 \text{ m s}^{-1}$ ) while  $t \leq 5$  days and is zero thereafter. The surface zonal wind stress  $\tau_s^\lambda$  is thus given by

$$\tau_s^\lambda(\lambda, \phi, t) = \begin{cases} \tau_0 \exp \left\{ - \left[ \left( \frac{\lambda - \lambda_0}{W_\lambda} \right)^2 + \left( \frac{\phi - \phi_0}{W_\phi} \right)^2 \right] \right\} & ; 0 \leq t \leq 5d \\ 0 & ; t > 5d \end{cases}$$

The spatial and temporal scale of this forcing is broadly characteristic of the MJO, as is the peak magnitude (Hendon et al. 1998). This experiment is qualitatively similar to that of McCreary et al. (1993), and Valsala (2008) who used a  $2\frac{1}{2}$  layer model to examine the response of the Indian Ocean to seasonal to interannual wind anomalies.

Figure 3(a) shows the model SSH anomalies for this control simulation after the initial five days of forcing. The positive SSH anomalies indicate a downwelling equatorial Kelvin wave being forced at  $75^\circ\text{E}$ , while the negative off-equatorial SSH anomalies indicate the upwelling Rossby wave response to the wind forcing. By day 35, the Kelvin wave has propagated eastwards, impinging on the coast of Sumatra where coastal waves are triggered along with reflected downwelling Rossby waves (Figure 3(b)). The coastally trapped waves propagate both northwards and southwards, with some of the energy from the latter portion propagating into the Maritime Continent. This energy spreads in all directions, with coastal wave signals propagating around the island coastlines (for example, the positive SSH anomalies along the east coast of Java and Sumatra and then along the west coast of Borneo) and through the various channels. The surface wave signal is not apparently dependent on channel depth and is capable of propagating through channels with a maximum depth of less than 20 m, such as between Borneo and Sumatra. Note that the vertical resolution is around 10 m in the surface layers of the model, so such waves will be imperfectly resolved in such shallow depths.

The subsequent westward propagation of the reflected Rossby wave along the off-equatorial waveguide can be seen in the transition from day 35 to 65 (Figure 3(b) to 3(c)), and is similar to that observed (Oliver and Thompson 2010; Webber et al. 2010). At the same time, the upwelling Rossby waves (negative SSH anomalies) have reached the coast of Africa and have begun to reflect into an upwelling equatorial Kelvin wave. The coastally trapped waves propagating along the northern coastal waveguide have circumnavigated the Bay of Bengal and the Arabian Sea, with the westernmost positive SSH anomalies reaching the southern coast of the Arabian Peninsula, as seen in models (Valsala 2008) and observations (Oliver

and Thompson 2010; Webber et al. 2010). The downwelling coastal wave which propagated southwards along the west coast of Australia has generated westward-propagating Rossby waves in the southern Indian Ocean while the anomalies that propagated through the Maritime Continent have formed a downwelling equatorial Kelvin wave in the Pacific (positive SSH anomalies at 140–160°E on the equator).

Figure 3(d) shows the eventual SSH anomalies at 95 days along with the propagation paths of the various wave responses. The thick black arrow shows the equatorial Kelvin waveguide and subsequently the northern coastal waveguide, emphasised because this waveguide retains energy within the tropical Indian Ocean. The thin black lines show the southern coastal waveguide including the path through the Lombok Straits into the Maritime Continent. The grey arrows and dashed boxes show the off-equatorial Rossby waveguide. The arrival of the downwelling equatorial Rossby wave in the western Indian Ocean can be seen in this figure (positive off-equatorial SSH anomalies at 45–60°E). Coastal Kelvin waves have propagated all the way around the northern coastal waveguide (shown by the thick black arrow) to arrive in the western Indian Ocean at the same time as the equatorial Rossby wave. Once they reach the equatorial region they may contribute to and reinforce the positive SSH anomalies there at around 100 days after the initial wind forcing; we return to this question later. The propagation and timing of both the equatorial Rossby and coastally trapped waves agrees well with observational composites of the free wave response to MJO forcing (Webber et al. 2010).

*b. Sensitivity to latitudinal width of westerly wind forcing*

The sensitivity of the ocean response to the latitudinal Gaussian decay scale ( $W_\phi$ ) of the wind patch is examined. Four experiments were carried out, with latitudinal decay scales of 20°, 10° (the control run), 5° and 1° (Figure 4). The peak amplitude  $\tau_0$  is the same for all four simulations ( $0.1 \text{ N m}^{-2}$ ), hence the wider wind bursts will input more total energy to the ocean, as well as projecting differently onto the equatorial wave meridional modes. As

would be expected, there are larger SSH signals away from the equator in the wider wind burst simulations, leading to stronger variability in the Bay of Bengal and the Arabian sea. However, in the equatorial waveguide the sign of the SSH anomalies changes between the simulations, with positive anomalies in the western Indian Ocean in the 20° experiment but predominantly negative SSH anomalies in the same region for the 1° and 5° simulations. The key result is therefore that the latitudinal decay scale of the westerly wind burst can alter not just the magnitude, but also the sign of the resulting equatorial anomalies 95 days later.

The relative strength of the various baroclinic modes (with their different vertical structures and zonal propagation speeds) is also different between the simulations. Within the equatorial waveguide, there are strong positive anomalies at 40–70°E and 80–90°E clearly separated zonally by negative anomalies at 70–80°E in the 20° experiment (Figure 4(a)), while narrower wind bursts lead to much less distinction and separation between the modes (zonally uniform negative near-equatorial anomalies in the 5° and 1° experiments). It therefore appears that varying the latitudinal decay scale of the wind forcing leads to a different combination of baroclinic and meridional modes in the model and subsequently a different equatorial SSH signal 95 days after the initial forcing. The implication is that a westerly wind burst at the equator needs to have a latitudinal decay scale greater than 5° latitude in order for the ocean forcing mechanism postulated by Webber et al. (2010) to be important.

*c. Sensitivity to stratification and bathymetry*

We now construct simulations with the same wind forcing as the control run but with varying bathymetry and stratification to examine the interaction between Kelvin and shelf wave modes along the coastal waveguide. The bathymetry is either the default model bathymetry used in the control run (see Figure 1) or a “flat” bathymetry, set to zero where shallower than 200 m and 4000 m elsewhere. The stratification is either the same as the control, or a two-layer stratification comprising the surface potential density ( $\rho_1 =$

1022.1 kg m<sup>-3</sup>) in the top 12 model levels ( $\sim 200$  m) and the bottom layer potential density ( $\rho_2 = 1027.8$  kg m<sup>-3</sup>) in the lower 28 model levels (Figure 1). For the two-layer configuration, we expect the ocean dynamics to consist solely of the barotropic and first baroclinic mode waves, with coastal waves resembling pure Kelvin waves. The propagation speed of the first baroclinic mode Kelvin wave for this configuration is

$$c_e = \sqrt{\frac{(\rho_2 - \rho_1)H_e}{\rho_1 g}} = 2.75 \text{ m s}^{-1},$$

where  $H_e$  is the equivalent depth, i.e., the depth of the surface density layer. This phase speed is in good agreement with the calculated first baroclinic mode equatorial Kelvin wave phase speed for the Indian Ocean, which is typically between 2.6 and 2.8 m s<sup>-1</sup> (Chelton et al. 1998). The estimated Kelvin wave phase speed for the model with full 40-layer stratification and the realistic (control run) bathymetry (Figure 2) is around 2.5 m s<sup>-1</sup>, so we expect the waves to propagate slightly faster in the two-layer configuration. To isolate the Kelvin wave response we construct Hovmöller diagrams along the equatorial Kelvin and coastal waveguides, as shown by the thick black arrow in Figure 3(d). Note that some of the reflected Rossby wave propagation can be seen in the equatorial waveguide but this Rossby wave signal is relatively weak.

The first experiment is the most idealised, with just the 2-layer stratification and flat bathymetry (Figure 5(a)). The downwelling first baroclinic mode Kelvin wave (positive SSH anomalies) propagates eastward along the equatorial waveguide to the coast of Sumatra (point B) then anticlockwise around the Bay of Bengal to the southern tip of India (point C) and onwards around the Arabian Sea to the Somali coast at the equator (point A). This propagation is very clear and coherent, with minimal energy loss. The arrival of the coastal Kelvin wave in the western Indian Ocean (point A) coincides almost perfectly with that of the reflected Rossby wave which can be seen to a certain extent in the equatorial waveguide (left hand side of Figure 5(a)). Interestingly, some of the energy initially associated with the upwelling equatorial Rossby waves escapes into the coastal waveguide near the tip of India (point C) where the coastal waveguide extends into the equatorial domain. There may also

be direct forcing of coastal waves here, although the along-shore component of the westerly wind forcing will be small.

After the initial downwelling coastal Kelvin wave there are several wave signals of both signs that can be seen propagating along the coastal waveguide. Some of these can be traced back to reflection of equatorial Rossby waves at the western boundary (point A); for example, the negative SSH anomalies here at around day 40 reflect into an upwelling equatorial Kelvin wave which reaches the eastern boundary (point B) around day 75. This signal then propagates coherently around the coastal waveguide as an upwelling equatorial Kelvin wave (negative SSH anomalies) to arrive just past point C at day 120. Similar behaviour can be seen in the downwelling wave signal (positive SSH anomalies) that reaches the western boundary around day 100, subsequently reflecting into an equatorial Kelvin wave that arrives at point B at day 120.

The effect of bathymetry is investigated by replacing the flat bathymetry with realistic sloping bathymetry (c.f. Figure 2), while keeping the idealised 2-layer stratification (Figure 5(b)). This experiment shows less coherent propagation along the coastal waveguide, whereas the equatorial propagation pattern in the open ocean (left hand portion of the diagrams) is almost identical. The sloping bathymetry will lead to coastal trapped waves with dispersive properties (Huthnance 1975; Brink 1982) and thus will attenuate the signal as it propagates around the coastal waveguide. Thus it is unsurprising that the downwelling Kelvin wave signal is relatively spread out and that the signal is weaker by the time it reaches the western Indian Ocean.

The effect of using a realistic 40-layer stratification, but reinstating the idealised flat bathymetry, is shown in Figure 5(c). The propagation of energy along the equatorial waveguide is much more spread out than in the idealised 2-layer stratification experiments (Figures 5(a,b)), probably due to the partitioning of wave energy between the multiple baroclinic modes that are now allowed by the model. The coastal wave propagation is clearly split into two baroclinic modes with different propagation speeds as shown by their relative slopes

on the Hovmöller diagrams. As expected, the wave propagation is slightly slower for this realistic stratification than for the two-layer configuration (Figure 5(a,b)), with the peak in positive SSH at the western boundary (point A) occurring 10–20 days later.

Finally, Figure 5(d) shows the corresponding Hovmöller diagram for the control simulation (as in Figure 3) with both realistic stratification and bathymetry. In this figure, the two factors of energy partitioning between baroclinic modes and increased energy dispersion along the coastal waveguide lead to quite a different picture from Figures 5(a–c). The two baroclinic modes evident in Figure 5(c) are no longer apparent. The propagation of the positive SSH anomalies along the equatorial waveguide is less coherent compared with Figure 5(b), with weaker positive SSH anomalies at the western boundary (point A) at days 100–120. In addition, the coastal wave signal spreads further in time and space than in the other simulations, and becomes insubstantial before arriving in the western Indian Ocean; the weak positive SSH signal on the equator at point A is primarily due to the Rossby wave propagation. Therefore, in the real ocean, it seems likely that the coastal waveguide will be less important than the equatorial Rossby waveguide for forcing MJO variability in the western Indian Ocean.

The simulations described above summarise the dynamical ocean response to idealised WWBs associated with the MJO in the Indian Ocean. This consists of a combination of equatorial Kelvin and Rossby waves along with coastally trapped waves. Some of the equatorial wave energy escapes along the southern coastal waveguide and into the Maritime Continent, which subsequently leads to weak equatorial Kelvin wave activity in the Pacific. The remainder returns across the Indian Ocean in the form of both equatorial Rossby waves and coastally trapped waves propagating along the northern coastal waveguide. For realistic simulations, the interaction of wave modes along the sloping bathymetry of this coastal waveguide leads to dissipation of this coastal signal before it arrives in the western Indian Ocean. In contrast, equatorial Rossby waves do propagate coherently across the width of the Indian Ocean, and arrive in the western Indian Ocean around 100 days after the

initial downwelling Kelvin wave was forced. There are also upwelling wave signals (negative SSH anomalies) that are approximately half a cycle out of phase with the downwelling waves. Multiple meridional and baroclinic wave signals are seen, the distribution of which partly depends upon the latitudinal decay scale of the initial wind forcing. The combination of these wave modes has the potential to critically alter the dynamic ocean state along the equatorial waveguide, and is thus crucial for determining the potential for triggering atmospheric convection and the MJO.

## 5. Realistic composite MJO wind forcing

The key processes in the dynamical ocean response to MJO-like wind forcing have been determined in the idealised experiments of section 4. In this section, the dynamical ocean response to realistic MJO wind forcing is examined. We force the model with composite MJO winds globally (see Section 2). These composites consist of eight global fields of the zonal and meridional components of the surface wind (one for each of the eight Wheeler-Hendon MJO phases), which are then interpolated onto a daily time scale by assuming a constant 6 day time interval between phases. This gives a 48-day cycle for the MJO, which is consistent with previous definitions of the MJO life-cycle (Madden and Julian 1972, 1994). However, this emphasises the cyclical component of the MJO which may not always be appropriate during periods of sporadic behaviour (Matthews 2008), and will tend to smear out some of the freely propagating oceanic wave signals generated (Webber et al. 2010). Nevertheless, it is useful as a tool to investigate the key components of the dynamical ocean response to the cyclical MJO. The simulation is run for two full cycles of the MJO (i.e., 96 days), to allow processes occurring over the time scale of multiple MJO cycles to be seen.

*a. Global SSH anomalies*

Figure 6 shows the SSH anomalies from the second MJO cycle of the simulation (i.e., day 54 to 96) in the left column, with the equivalent composites of observed SSH anomalies in the right hand column. In general the agreement between the model and observations is strikingly good. There is more small-scale noise in the observations, which is to be expected as the model is forced by the relatively low resolution  $1^\circ$  ECMWF winds (compared with the  $0.25^\circ$  SSH data) and does not contain currents and their associated eddies. The propagation of waves around the Indian Ocean in the model shows all the same features as the observations, as does the propagation of SSH anomalies into the Maritime Continent. Several of the features evident in the idealised westerly wind burst experiment (Figure 3) are also evident in this composite simulation; the reflection of equatorial waves at the eastern boundary is similar, as is the propagation of waves around the coastal waveguide.

The modelled propagation of Kelvin waves across the equatorial Pacific appears consistent with observations, although the subsequent generation of coastal waves and reflected Rossby waves at the eastern boundary is stronger and more coherent in the model than in observations. There is also evidence in the model of equatorial Kelvin wave activity in the Atlantic, which is somewhat evident but less clear in the observations. A role for the MJO in forcing dynamical variability in the Atlantic has been postulated previously, but not proven (Foltz and McPhaden 2004; Han et al. 2008; Webber et al. 2010). Our results indicate that at least a portion of this observed variability arises through wind forcing associated with the MJO.

The conclusion of this simulation is that the majority of the observed SSH variability composited relative to the MJO can be explained by the linear dynamical response to surface wind forcing. This implies that other, non-linear processes are less important, although they may account for the decay in the equatorial Kelvin wave signals as they propagate across the Pacific. There are also large coherent regions of SSH anomalies outside of the equatorial waveguide in the Pacific, in both hemispheres. Additionally, the model simulates

the relatively large ( $>1.5$  cm) variability of SSH in the Red Sea noted by Webber et al. (2010). The positive SSH anomalies in phase 7 coincides with strong south-easterly wind anomalies over the preceding two MJO phases (not shown) which will lead to anomalous inflow of water into the Red Sea and thus raise the sea surface; the reverse process accounts for the negative SSH anomalies in phase 3. The variability in the Gulf of Carpentaria found by Oliver and Thompson (2011) and in the observational composites here is not reproduced in quite the same manner; the observed strong positive (negative) SSH anomalies in phases 6–7 (2–3) correspond to a dipole pattern of SSH anomalies in the model. It is not clear what causes this discrepancy, but it may be due to inaccurate representation of the shallow bathymetry of the area in the model, or due to other surface processes not included in this model.

## **6. Realistic primary Madden-Julian event wind forcing experiment**

We now move to the question of how ocean dynamics might force primary Madden-Julian (MJ) events. Webber et al. (2011) investigated this question using a combination of composite and case study analysis applied to observational data. Here, we will examine their case study of the primary event starting on 24 September 2004 in further detail, by attempting to simulate the oceanic equatorial Rossby wave activity that preceded the triggering of this event. Four experiments are run. The first uses the observed winds for the 150 days previous to the start of the primary MJ event to drive the ocean circulation, i.e., wind forcing from 27 April 2004. The later experiments use the winds for the 120 days, 50 days and 30 days previous to the start of the primary MJ event, respectively. This will allow insight into the key components of the atmospheric forcing necessary to generate this oceanic equatorial Rossby wave.

*a. 150 day experiment*

Figure 7(a) shows the observed SSH and SST anomalies in the off-equatorial Rossby waveguide for the 100 days prior to the initiation of the event of 24 September 2004, until 10 days after the event. Note that day zero of the primary event (i.e., 24 September 2004) is defined to be the maximum principal component amplitude during “phase A” of the MJO, following the definition of Matthews (2008). Therefore, the actual initiation of the convection associated with this MJ event occurs around 10–15 days earlier, as shown by the OLR anomalies (dashed contours in Figure 7(b)).

The arrival of the downwelling Rossby wave in the western Indian Ocean can be clearly seen in Figure 7(a), as can the resultant positive SST anomalies, as shown by the diagonally-oriented solid contours in the western Indian Ocean between days  $-60$  and  $+10$ . The location and timing of the warm SST anomalies agree well with the initiation of the convective anomalies associated with the primary MJ event (dashed contours in (b)). There are likely to be other factors influencing the triggering of this event. For example, there are cold SST anomalies (dashed contours in Figure 7(a)) in the eastern Indian Ocean that are associated with suppressed convection in this region that may induce circulation that is favourable for the initiation of convection in the western Indian Ocean. In addition, there is some evidence for a weak convective signal that circumnavigates the globe following the convective activity in the Pacific at lag  $-50$  (not shown) and may also be favourable for the triggering of the event. Nevertheless, given the strength of the dynamically-induced SST anomalies, it seems reasonable to conclude that the arrival of the downwelling Rossby wave has a role in triggering this primary MJ event, following the arguments of Webber et al. (2010, 2011).

When the model is forced using observed winds over the 150 days prior to the primary event of 24 September 2004, it is able to simulate the observed wave propagation with reasonable accuracy (compare SSH anomalies in panels (a) and (b) in Figure 7). The magnitude of the SSH anomalies is somewhat smaller in the simulation than in the observations, but the pattern of anomalies agrees well, albeit with less small-scale noise than the observations.

These differences may be due to erroneous noise in the observations, to genuine variability not captured in the temporally filtered  $1^\circ$  wind forcing, or possibly to variations in the propagation speed of the Rossby waves between the model and observations. There appear to be two distinct downwelling Rossby wave signals: one (wave A) which is triggered by reflection of the downwelling Kelvin wave arriving at the eastern boundary (Figure 7(d)), and a later one (wave B) that begins near the eastern boundary at day  $-60$  and appears to be augmented by local wind forcing around day  $-40$ . The combination of these waves appears to generate the broad region of positive SSH anomalies in the western Indian Ocean around days  $-20$  to  $-10$ . The latter wave (wave B) continues to propagate westwards after the MJ event is triggered, and is further amplified following the subsequent easterly winds (days  $+10$  to  $+30$ ; not shown). However, wave B may be somewhat less important than wave A for triggering the primary event itself, judging by the location at which convection is triggered (west of  $50^\circ\text{E}$  at day  $-10$ ).

*b. Re-emergence of dynamical ocean anomalies*

Analysis of the zonal wind averaged over  $10^\circ\text{N}$ – $10^\circ\text{S}$  in the Indian Ocean (Figure 7(c)) shows that there was a long interval of relatively weak equatorial winds during boreal summer (approximately day  $-120$  to  $-50$ ), with only a slight increase in variability in the 50 days preceding the primary event. However, around day  $-140$  there was a large westerly wind burst, especially intense in the region of  $70$ – $80^\circ\text{E}$  (black line in Figure 7(c)). This appears to be linked to the triggering of the downwelling equatorial Kelvin wave shown in Figure 7(d). The winds remain westerly for a period of 20 days after this wave is triggered, further intensifying the signal.

There is also an easterly wind burst around day  $-40$  which may be partly responsible for the intensification and rapid westward propagation of wave B around day  $-40$  in Figure 7(b). It is likely that the period of relative quiescence between days  $-120$  and day  $-40$  is partly due to the northward displacement of the monsoonal circulation and MJO during boreal

summer (Wang and Rui 1990). The westerly wind burst which triggers the initial equatorial Kelvin wave is thus probably associated with the last major MJO cycle of the boreal spring season (140 days prior to 24 September is 7 May).

A key result is therefore that a westerly wind burst in the central Indian Ocean associated with a strong MJ event can trigger equatorial wave activity in the Indian Ocean that can affect the MJO 140 days (approximately five months) later. This is associated with the “re-emergence” of SST anomalies generated by ocean dynamics forced by wind variability during the preceding boreal spring and subsequently leading to convective anomalies. 140 days is an extraordinary lead time for the MJO, for which predictability is normally limited to around three weeks (Love and Matthews 2009; Kang and Kim 2010; Vitart and Molteni 2010; Rashid et al. 2011). Thus, even the relatively short lead time associated with the easterly wind forcing at day  $-40$  suggests the potential for unprecedented predictability.

*c. Sensitivity to length of wind forcing history*

Although we have clearly shown that 150 days of wind forcing simulates the observed wave propagation preceding the primary MJ event of 24 September 2004, it remains an open question whether it is possible to simulate similar dynamics with a shorter period of wind forcing. It is possible that a similar SSH structure could be generated without the westerly wind burst at  $-140$  days. We now turn to this question by examining Hovmöller diagrams of Rossby wave propagation from such model simulations integrated over a shorter period of wind forcing (Figure 8). The observed SSH anomalies are reproduced in each panel to facilitate comparison. The run with 150 days of wind forcing (Figure 8(a)) shows that the model SSH anomalies agree broadly with the location of the observed anomalies, although the fit is not exact, as discussed above.

When the model is forced only with observed winds over the preceding 120 days (Figure 8(b)), there is little if any evidence of the Rossby wave generated by reflection at the western boundary in panel (a). This is unsurprising given that this wave can be traced back

to wind forcing that occurred before the 120 day cut-off. There are some positive SSH anomalies along the propagation path of wave A, which may be locally forced, but these do not propagate coherently as a Rossby wave. However, there is evidence of an upwelling Rossby wave which propagates from the eastern Indian Ocean before being largely over-ridden by the broad region of positive SSH anomalies between  $60^\circ$  and  $90^\circ\text{E}$ , associated with wave B and forced by the easterly wind anomalies around day  $-40$ . The positive SSH anomalies associated with this downwelling wave (wave B) do propagate relatively coherently, but do not create a broad region of positive SSH anomalies between days  $-20$  and  $-10$ , in time for triggering the primary event.

Panels (c) and (d) show the results from shorter simulations. For the simulation with 50 days (Figure 8(c)), wave B is strongly evident; more so than for the 120 day simulation since the preceding upwelling Rossby wave is not simulated. The SSH anomalies do not agree well with the location and timing of the observed SST anomalies but could still have a role in enhancing the convective anomalies of the primary MJ event. However, from Figure 8(d), it is clear that 30 days of wind forcing is not sufficient to generate any positive SSH anomalies locally in the western Indian Ocean. We therefore conclude that the ocean dynamics are not merely a response to wind forcing in the few weeks before the primary event, but rather a response to wind forcing from more than a month before. Furthermore, the role of the westerly wind burst five months previously is confirmed as being important to the triggering of the primary event.

#### *d. Rossby wave vertical structure*

We now analyse the vertical structure of the model Rossby waves in order to investigate the magnitude of the thermocline displacement associated with the SSH perturbations. Figure 9 shows depth-longitude sections for the surface 450 m over  $45\text{--}95^\circ\text{E}$  in both our model and “observations” from the ECCO ocean state estimate (Wunsch and Heimbach 2007). In both the model and observations, the downwelling wave can be traced in the form of negative

density anomalies back to the eastern boundary at day  $-100$ . These anomalies are maximum around 100 m depth but extend coherently into the deep ocean with a slight westward tilt with increasing depth. This tilt implies upward phase propagation and downward energy propagation and has been observed in equatorial Kelvin waves for the Pacific Ocean forced by the MJO (Matthews et al. 2007, 2010). The coherent propagation across the width of the Indian Ocean reinforces the hypothesis that the wave activity can be traced back to reflection of the equatorial Kelvin wave incident on the eastern boundary prior to day  $-100$ .

One difference between the model and the observations is in the near-surface density anomalies, especially in days  $-60$  to  $0$ . The model shows a persistent surface layer of positive density anomalies overlying the negative density anomalies associated with the downwelling Rossby wave, while this layer is much more broken in the observations. This is likely to be associated with surface thermodynamic and precipitation processes not included in our simulations, which will act to modify the density of the surface layers. In addition, non-linear processes and mixing by near-surface currents are not present in the model and may also play a role.

## 7. Discussion

### *a. Ocean Dynamics*

Our results show that the observed wave propagation can be simulated by a simple ocean model linearised about a resting basic state. This realistic behaviour is evident even from model simulations forced by an idealised Gaussian westerly wind burst on the equator in the Indian Ocean. The subsequent wave propagation shows many of the features identified in previous studies of the dynamics of this ocean basin in response to wind forcing by the MJO (Oliver and Thompson 2010; Webber et al. 2010). Crucially, the arrival of downwelling oceanic equatorial Rossby waves in the western Indian Ocean around 90 days after the initial wind burst agrees with the findings of Webber et al. (2010) and with hypotheses of coupling

between the atmosphere and the ocean dynamics on such time scales (Han et al. 2001; Han 2005; Fu 2007). The western Indian Ocean is an important region in which forcing by oceanic equatorial Rossby waves can influence atmospheric convection due to the relatively shallow thermocline, higher rates of entrainment cooling (McCreary et al. 1993) and thus increased correlation between SSH and SST anomalies (Xie et al. 2002). It is worth noting that the model does not contain the complex equatorial current systems of the Indian Ocean, which would be expected to alter the phase speed of Rossby waves through Doppler shifting and by altering the meridional vorticity gradient through which they propagate (McPhaden and Ripa 1990). Therefore the location of the waves in time and space may vary between model and observations.

The model reproduces the observed propagation of coastally trapped waves, both southwards along the coasts of Sumatra and Java into the Maritime Continent and northwards around the Bay of Bengal. This latter coastal waveguide continues around the tip of India, where wave energy may escape from the equatorial waveguide or be triggered by near-equatorial winds. Coastally trapped waves continue to propagate around the Arabian seas and arrive in the western Indian Ocean at around the same time as the equatorial Rossby waves. This coincidence in timing led Webber et al. (2010) to hypothesise that the propagation of anomalies along the coastal waveguide could contribute to feedbacks onto the MJO. This hypothesis is consistent with the results of a two layer model with flat bathymetry, in which the coastal Kelvin wave arrives at the same time as the equatorial Rossby wave. However, simulations with more realistic stratification and bathymetry suggest that interactions between baroclinic modes and barotropic shelf wave modes lead to higher levels of energy dispersion such that the coastally trapped wave signal never reaches the western Indian Ocean. Therefore we can conclude that it is the oceanic equatorial Rossby wave dynamics that are important for understanding coupling between the MJO and the dynamics of the Indian Ocean.

Another constraint on the potential for feedbacks from the ocean dynamics onto the MJO

appears to be the latitudinal decay scale of the westerly wind burst which generates the initial wave activity. In order for the eventual SSH anomalies to be coherent, it appears that the Gaussian westerly wind burst must have a latitudinal decay scale greater than  $5^\circ$  ( $10^\circ$  is certainly sufficient). Narrower wind bursts change not just the magnitude but also the sign of the eventual equatorial anomalies, with substantially altered spatial patterns for the SSH anomalies. It is hypothesised that this difference between the simulations is due to different projections of the initial wind forcing onto meridional and baroclinic wave modes. This variation in the dynamic response suggests that atmospheric variability needs to be coherent over a relatively broad latitudinal range, centred on the equator, in order to effectively force dynamical variability in the equatorial oceans. In addition, the boreal summer MJO, which exhibits less coherent variability around the equator (Wang and Rui 1990) will probably be less effective in forcing such dynamics.

When the model is forced by realistic composite MJO winds globally, it is able to replicate the observed composite SSH anomalies. This is an important result as it reinforces the notion that the global SSH response to the MJO is a simple product of the linear dynamic response to surface momentum flux; non-linear and thermodynamic effects are not required and neither is a realistic ocean circulation. We might therefore infer that the interannual variability of the ocean will have a relatively minor effect on the dynamical ocean response to the MJO which will be predominantly a linear addition to this low-frequency variability.

In addition, this model run highlights some intriguing characteristics of the global dynamic ocean response to the MJO. For example, there is evidence of equatorial Kelvin wave propagation in the Atlantic which subsequently can be seen to propagate in both directions along the coast of Africa. Such behaviour has been seen by Polo et al. (2008), but has not previously been attributable to the MJO; our results suggest that at least a portion of this can be attributed to a local linear response to wind variability associated with the MJO. The model also simulates substantial SSH variability in the Red Sea, in agreement with observations (Webber et al. 2010) but fails to simulate the observed SSH variability in the

Gulf of Carpentaria (Oliver and Thompson 2011). Such forms of local variability are likely to have a substantial impact on biological productivity due to variations in the upwelling of nutrients. This would build upon existing research that has established a role for the MJO in generating chlorophyll variability through such mechanisms (Waliser et al. 2005; Isoguchi and Kawamura 2006).

*b. Primary Events*

A model simulation with observed winds over the 150 days preceding the primary MJ event of 24 September 2004 reproduces closely the observed SSH variability which has previously been implicated in triggering this primary event (Webber et al. 2011). A westerly wind burst 140 days before the primary event is implicated in generating a downwelling Kelvin wave which subsequently reflects into the first of two Rossby wave signals seen (wave A). This wave propagates westwards to arrive in the western Indian Ocean shortly before the initiation of convection, although there is a slight difference in the propagation speed of this wave between model and observations. Simulations with shorter periods of wind forcing are less successful at replicating the observed dynamics, although 50 days is sufficient to generate the latter portion of the wave activity observed (wave B). From the observations of SST and OLR, it appears that wave A is at least as important as wave B (indeed, probably more so) in generating the warm SST anomalies which prime the atmosphere for convection. The reduced convection in the eastern Indian Ocean that precedes the initiation of the primary event may also be influential through modifications to the atmospheric circulation; these reduced convective anomalies coincide with cold SST anomalies that may be partly driven by the preceding upwelling Rossby wave.

To put these forcing events into context, Figure 10 shows the intraseasonal OLR anomalies averaged over  $15^{\circ}\text{N}$ – $15^{\circ}\text{S}$  for the period from 150 days prior to 30 days after the primary event of 24 September 2004. The westerly wind burst around day  $-140$  can be clearly linked to intense convective activity over the eastern Indian Ocean region (negative OLR values

below  $-25 \text{ W m}^{-2}$  between  $65\text{--}100^\circ\text{E}$  in early May). This is one of the last strong cycles of MJO activity of the boreal spring season, which is followed by relatively weak and incoherent anomalies during the summer season when convection shifts north of the equator (Wang and Rui 1990). The MJO becomes organised again in a cyclical sense in late September and early October. This re-invigoration of the MJO begins with the primary event on 24 September, which coincides with the re-emergence of ocean anomalies forced by a westerly wind burst before the summer period. There may also be a role for atmospheric variability, including the component of the MJO that exists to the north of the equator over the summer months, but it seems likely that the ocean dynamics at least play a role in triggering the primary event in question.

The key conclusion of this paper is therefore that the ocean dynamics act to integrate intraseasonal wind forcing over as much as five months and can subsequently trigger a primary MJ event. In the case study of 24 September 2004, the wave activity is triggered by the last major episode of MJO variability before the summer season. The equatorial waves propagate almost freely back and forth across the Indian Ocean, before being reinforced by a second Rossby wave, triggered by easterly wind anomalies around 40 days prior to the primary event. Thus an MJ event is able to influence another one four cycles later. Although we have only presented results from one case study, composite analysis suggests that downwelling Rossby waves are consistently important for triggering primary MJ events (Webber et al. 2011). Therefore, although the specifics will vary, it is likely that interaction between intraseasonal atmospheric variability and the ocean dynamics, with their differing time scales, is at least partly responsible for the sporadic nature of the MJO.

This potential for coupling between the intraseasonal atmospheric variability and dynamic ocean processes occurring at a longer time scale also brings the potential for forecasting MJO activity at long lead times. Given that current state-of-the-art forecasts of the MJO only exhibit skill up to 20–25 days (Love and Matthews 2009; Rashid et al. 2011), a process which is predictable over 140 days is exceptional. The degree to which the ocean dynamics

can be used to forecast the MJO remains to be tested, but it is likely to be strongest during periods of reduced MJO activity, when forecast skill is low (Jones et al. 2004). These results emphasise the importance of monitoring the equatorial Indian Ocean using combinations of moored buoys and ARGO floats, in combination with satellite data, to potentially facilitate such predictability.

*Acknowledgments.*

The altimeter products were produced by Ssalto/Duacs and distributed by Aviso with support from Cnes and are available at [www.aviso.oceanobs.com/](http://www.aviso.oceanobs.com/). The TMI SST data were obtained from the SSM/I website at [www.ssmi.com/tmi/](http://www.ssmi.com/tmi/). The EMCWF surface wind data were obtained through the British Atmospheric Data Centre (BADC) and from the ECMWF website at [data-portal.ecmwf.int/data/d/interim\\_daily](http://data-portal.ecmwf.int/data/d/interim_daily). The interpolated OLR data were obtained from the NOAA/OAR/ESRL PSD web site at [www.cdc.noaa.gov/](http://www.cdc.noaa.gov/). Data from the ECCO-GODAE project were obtained through the ftp site [www.ecco-group.org/](http://www.ecco-group.org/). The Wheeler-Hendon index was obtained from <http://www.bom.gov.au/>. BGMW was supported by a NERC PhD studentship.

# REFERENCES

## References

- Anderson, D. L. T., K. Bryan, A. E. Gill, and R. C. Pacanowski, 1979: The transient response of the North Atlantic: some model studies. *J. Geophys. Res.* **84**, 4795–4815.
- Battisti, D. S., 1988: Dynamics and thermodynamics of a warming event in a coupled tropical atmosphere ocean model. *J. Atmos. Sci.* **45**, 2889–2919.
- Brink, K. H., 1982: A comparison of long coastal trapped wave theory with observations off Peru. *J. Phys. Oceanogr.* **12**, 897–913.
- Brink, K. H., 1991: Coastal-trapped waves and wind-driven currents over the continental-shelf. *Annu. Rev. Fluid Mech.* **23**, 389–412.
- Chelton, D. B., R. A. DeSzoeko, M. G. Schlax, K. El Naggar, and N. Siwertz, 1998: Geographical variability of the first baroclinic Rossby radius of deformation. *J. Phys. Oceanogr.* **28**, 433–460.
- Chelton, D. B., and M. G. Schlax, 1996: Global observations of oceanic Rossby waves. *Science* **272**, 234–238.
- Chelton, D. B., M. G. Schlax, J. M. Lyman, and G. C. Johnson, 2003: Equatorially trapped Rossby waves in the presence of meridionally sheared baroclinic flow in the Pacific Ocean. *Prog. Oceanog.* **56**, 323–380.
- Ducet, N., P. Y. Le Traon, and G. Reverdin, 2000: Global high-resolution mapping of ocean circulation from TOPEX/Poseidon and ERS-1 and-2. *J. Geophys. Res.* **105**, 19477–19498.

- Foltz, G. R., and M. J. McPhaden, 2004: The 30-70 day oscillations in the tropical Atlantic. *Geophys. Res. Lett.* **31**, L15205. doi: 10.1029/2004GL020023.
- Fu, L. L., 2007: Intraseasonal variability of the equatorial Indian Ocean observed from sea surface height, wind, and temperature data. *J. Phys. Oceanogr.* **37**, 188–202.
- Fu, L. L., E. J. Christensen, C. A. Yamarone, M. Lefebvre, Y. Menard, M. Dorrer, and P. Escudier, 1994: TOPEX/Poseidon mission overview. *J. Geophys. Res.* **99**, 24369–24381.
- Gentemann, C. L., F. J. Wentz, C. A. Mears, and D. K. Smith, 2004: In situ validation of Tropical Rainfall Measuring Mission microwave sea surface temperatures. *J. Geophys. Res.* **109**, C04021. doi: 10.1029/2003JC002092.
- Giese, B. J., and D. E. Harrison, 1990: Aspects of the Kelvin wave response to episodic wind forcing. *J. Geophys. Res.* **95**, 7289–7312.
- Han, W., 2005: Origins and dynamics of the 90-day and 30-60-day variations in the equatorial Indian Ocean. *J. Phys. Oceanogr.* **35**, 708–728.
- Han, W., D. M. Lawrence, and P. J. Webster, 2001: Dynamical response of equatorial Indian Ocean to intraseasonal winds: zonal flow. *Geophys. Res. Lett.* **28**, 4215–4218.
- Han, W., P. J. Webster, J. L. Lin, T. Liu, R. Fu, D. Yuan, and A. Hu, 2008: Dynamics of intraseasonal sea level and thermocline variability in the equatorial Atlantic during 2002–03. *J. Phys. Oceanogr.* **38**, 945–967.
- Hendon, H. H., B. Liebman, and J. D. Glick, 1998: Oceanic Kelvin waves and the Madden Julian oscillation. *J. Atmos. Sci.* **55**, 88–101.
- Huthnance, J. M., 1975: Trapped waves over a continental-shelf. *J. Fluid Mech.* **69**, 689–704.
- Isoguchi, O., and H. Kawamura, 2006: MJO-related summer cooling and phytoplankton blooms in the South China Sea in recent years. *Geophys. Res. Lett.* **33**, L16615. doi:

10.1029/2006GL027046.

- Jones, C., L. M. V. Carvalho, R. W. Higgins, D. E. Waliser, and J. K. E. Schemm, 2004: A statistical forecast model of tropical intraseasonal convective anomalies. *J. Climate* **17**, 2078–2095.
- Kang, I., and H. Kim, 2010: Assessment of MJO Predictability for Boreal Winter with Various Statistical and Dynamical Models. *J. Climate* **23**, 2368–2378.
- Kessler, W. S., and M. J. McPhaden, 1995: Oceanic equatorial waves and the 1991-93 El-Nino. *J. Climate* **8**, 1757–1774.
- Kessler, W. S., M. J. McPhaden, and K. M. Weickmann, 1995: Forcing of intraseasonal Kelvin waves in the equatorial Pacific. *J. Geophys. Res.* **100**, 10,613–10,631.
- Kummerow, C., J. Simpson, O. Thiele, W. Barnes, A. T. C. Chang, E. Stocker, R. F. Adler, A. Hou, R. Kakar, F. Wentz, P. Ashcroft, T. Kozu, Y. Hong, K. Okamoto, T. Iguchi, H. Kuroiwa, E. Im, Z. Haddad, G. Huffman, B. Ferrier, W. S. Olson, E. Zipser, E. A. Smith, T. T. Wilheit, G. North, T. Krishnamurti, and K. Nakamura, 2000: The status of the Tropical Rainfall Measuring Mission (TRMM) after two years in orbit. *J. Appl. Met.* **39**, 1965–1982.
- Le Traon, P. Y., G. Dibarboure, and N. Ducet, 2001: Use of a high-resolution model to analyze the mapping capabilities of multiple-altimeter missions. *J. Atmos. Ocean. Tech.* **18**, 1277–1288.
- Liebmann, B., and C. A. Smith, 1996: Description of a complete (interpolated) outgoing longwave radiation dataset. *Bull. Am. Meteorol. Soc.* **77**, 1275–1277.
- Love, B. S., and A. J. Matthews, 2009: Real-time localised forecasting of the Madden-Julian Oscillation using neural network models. *Quart. J. Roy. Meteorol. Soc.* **135**, 1471–1483.
- Madden, R. A., and P. R. Julian, 1971: Detection of a 40-50 day oscillation in zonal wind

- in the tropical Pacific. *J. Atmos. Sci.* **28**, 702–708.
- Madden, R. A., and P. R. Julian, 1972: Description of global-scale circulation cells in the tropics with a 40-50 day period. *J. Atmos. Sci.* **29**, 1109–1123.
- Madden, R. A., and P. R. Julian, 1994: Observations of the 40-50 day oscillation, a review. *Mon. Weath. Rev.* **122**, 814–836.
- Matthews, A. J., 2000: Propagation mechanisms for the Madden-Julian oscillation. *Quart. J. Roy. Meteorol. Soc.* **126**, 2637–2651.
- Matthews, A. J., 2008: Primary and successive events in the Madden-Julian oscillation. *Quart. J. Roy. Meteorol. Soc.* **134**, 439–453.
- Matthews, A. J., P. Singhruck, and K. J. Heywood, 2007: Deep ocean impact of a Madden-Julian oscillation observed by Argo floats. *Science* **318**, 1765–1768.
- Matthews, A. J., P. Singhruck, and K. J. Heywood, 2010: Ocean temperature and salinity components of the Madden-Julian oscillation observed by Argo floats. *Clim. Dyn.* **35**, 1149–1168.
- McCreary, J. P., 1983: A model of tropical ocean-atmosphere interaction. *Mon. Weath. Rev.* **111**, 370–387.
- McCreary, J. P., P. K. Kundu, and R. I. Molinari, 1993: A numerical investigation of dynamics, thermodynamics and mixed-layer processes in the Indian-Ocean. *Prog. Oceanog.* **31**, 181–244.
- McPhaden, M. J., 1999: Genesis and evolution of the 1997–98 El Niño. *Science* **283**, 950–954.
- McPhaden, M. J., F. Bahr, Y. Dupenhoat, E. Firing, S. P. Hayes, P. P. Niiler, P. L. Richardson, and J. M. Toole, 1992: The response of the western equatorial Pacific-Ocean to westerly wind bursts during November 1989 to January 1990. *J. Geophys. Res.* **97**,

14289–14303.

- McPhaden, M. J., and P. Ripa, 1990: Wave–mean flow interactions in the equatorial ocean. *Annu. Rev. Fluid Mech.* **22**, 167–205.
- Oliver, E. C. J., and K. R. Thompson, 2010: Madden-Julian Oscillation and sea level: Local and remote forcing. *J. Geophys. Res.* **115**, C01003. doi: 10.1029/2009JC005337.
- Oliver, E. C. J., and K. R. Thompson, 2011: Sea level and circulation variability of the Gulf of Carpentaria: Influence of the Madden-Julian Oscillation and the adjacent deep ocean. *J. Geophys. Res.* **116**, . doi: 10.1029/2010JC006596.
- Polo, I., A. Lazar, B. Rodriguez-Fonseca, and S. Arnault, 2008: Oceanic Kelvin waves and tropical Atlantic intraseasonal variability: 1. Kelvin wave characterization. *J. Geophys. Res.* **113**, C07009. doi: 10.1029/2007JC004495.
- Rashid, H. A., H. H. Hendon, M. C. Wheeler, and O. Alves, 2011: Prediction of the Madden-Julian oscillation with the POAMA dynamical prediction system. *Clim. Dyn.* **36**, 649–661.
- Salby, M. L., and H. H. Hendon, 1994: Intraseasonal behavior of clouds, temperature, and motion in the tropics. *J. Atmos. Sci.* **51**, 2207–2224.
- Valsala, V., 2008: First and second baroclinic mode responses of the tropical Indian Ocean to interannual equatorial wind anomalies. *J. Oceanog.* **64**, 479–494.
- Vitart, F., and F. Molteni, 2010: Simulation of the Madden-Julian Oscillation and its teleconnections in the ECMWF forecast system. *Quart. J. Roy. Meteorol. Soc.* **136**, 842–855.
- Waliser, D. E., R. Murtugudde, P. Strutton, and J. L. Li, 2005: Subseasonal organization of ocean chlorophyll: Prospects for prediction based on the Madden-Julian Oscillation. *Geophys. Res. Lett.* **32**, . doi: 10.1029/2005GL024300.
- Wang, B., and H. Rui, 1990: Synoptic climatology of transient tropical intraseasonal con-

- vection anomalies - 1975-1985. *Meteorol. Atmos. Phys.* **44**, 43–61.
- Webb, D. J., 1996: An ocean model code for array processor computers. *Computers & Geosciences* **22**, 569–578.
- Webber, B. G. M., A. J. Matthews, and K. J. Heywood, 2010: A dynamical ocean feedback mechanism for the Madden-Julian Oscillation. *Quart. J. Roy. Meteorol. Soc.* **136**, 740–754.
- Webber, B. G. M., A. J. Matthews, K. J. Heywood, and D. P. Stevens, 2011: Ocean Rossby waves as a triggering mechanism for primary Madden-Julian events. *Quart. J. Roy. Meteorol. Soc.* In press.
- Wheeler, M. C., and H. H. Hendon, 2004: An all-season real-time multivariate MJO index: Development of an index for monitoring and prediction. *Mon. Weath. Rev.* **132**, 1917–1932.
- Wunsch, C., 1997: The vertical partition of oceanic horizontal kinetic energy. *J. Phys. Oceanogr.* **27**, 1770–1794.
- Wunsch, C., and P. Heimbach, 2007: Practical global oceanic state estimation. *Physica D* **230**, 197–208.
- Xie, S. P., H. Annamalai, F. A. Schott, and J. P. McCreary, 2002: Structure and mechanisms of South Indian Ocean climate variability. *J. Climate* **15**, 864–878.
- Zhang, C. D., 2005: Madden-Julian oscillation. *Rev. Geophys.* **43**, RG2003.

## List of Figures

- 1 Potential density profiles used as the model initial conditions. Solid line: default 40 level density profile, calculated from Levitus et al. (2002); Dashed line: two-layer density configuration. 36
- 2 Model bathymetry at  $1/3^\circ$  resolution (depth shaded in m; see legend). Labels refer to regions mentioned in this study. 37
- 3 SSH anomalies (cm) from the control run of the idealised westerly wind burst experiment. (a) day 5, (b) day 35, (c) day 65, (d) day 95. The equatorial wind patch forcing is indicated schematically by the dashed ellipse in (a). In (d), the equatorial and northern coastal Kelvin-waveguide is shown by the thick black line, the southern coastal waveguides by thin black lines and the equatorial Rossby waveguide by the grey arrows and dashed boxes. 38
- 4 SSH anomalies (cm) at day 95 for idealised westerly wind burst integrations with differing latitudinal decay scales of the initial wind patch forcing, shown schematically by the dashed ellipses. (a)  $20^\circ$ , (b) control run;  $10^\circ$ , (c)  $5^\circ$ , (d)  $1^\circ$ . 39
- 5 Hovmöller diagrams of SSH (cm) along the equatorial and coastal Kelvin-waveguides, as shown by the thick black line in Figure 3(d). (a) 2-layer model with flat bathymetry, (b) 2-layer model with sloping bathymetry, (c) full stratification but flat bathymetry, (d) full model with sloping bathymetry. The transition between the equatorial and coastal waveguides is at 5800km, as shown by the black vertical lines. The letters A, B, C along the top axes correspond to the locations marked in Figure 3(d). 40
- 6 SSH anomalies (cm) (a–h) from the model run with cyclical composite surface wind forcing, taken from days 54–96, corresponding to a full MJO cycle. (i–p) Composite SSH anomalies (cm) from satellite altimetry observations for the equivalent MJO phases. 41

- 7 (a) Hovmöller diagram of observed off-equatorial SSH (cm; shaded, see legend) and SST anomalies (contoured at  $\pm 0.3^\circ\text{C}$ , negative contour dashed) averaged over  $2\text{--}5^\circ\text{N}$  and  $2\text{--}5^\circ\text{S}$  for the 100 days preceding the primary event of 24 September 2004. (b) Hovmöller diagram of off-equatorial SSH from the model run forced by observed winds for the 150 days preceding the primary MJ event and observed equatorial ( $5^\circ\text{S}\text{--}5^\circ\text{N}$ ) OLR anomalies (contoured at  $\pm 15 \text{ W m}^{-2}$ , negative contour dashed) from day  $-100$  to  $+10$ . (c) Surface zonal wind stress anomalies ( $\text{Nm}^{-2}$ ) averaged over  $10^\circ\text{N}\text{--}10^\circ\text{S}$  and:  $40\text{--}100^\circ\text{E}$  (red line);  $70\text{--}80^\circ\text{E}$  (black line). (d) Hovmöller diagram of equatorial ( $2^\circ\text{N}\text{--}2^\circ\text{S}$ ) SSH from the same model run as (b) but for days  $-150$  to  $-100$ . 42
- 8 Hovmöller diagrams of model SSH (cm; shaded, see legend) and observed SSH anomalies (contoured at  $\pm 1 \text{ cm}$ , negative contour dashed) for the 100 days preceding the primary event on 24 September 2004. The model integrations were forced with observed wind stress, and started at (a) 150 days, (b) 120 days, (c) 50 days, (d) 30 days prior to the start of the primary MJ event on 24 September 2004 (day 0). 43
- 9 Vertical profiles of density anomalies ( $\text{kg m}^{-3}$ ; shaded, see legend) for the 100 days preceding the primary event on 24 September 2004 in: (a–f) the model simulation forced by observed winds over the 150 days prior to the primary event; (g–l) “observations” from the ECCO-GODAE ocean state estimation. (a,g) day  $-100$ , (b,h) day  $-80$ , (c,i) day  $-60$ , (d,j) day  $-40$ , (e,k) day  $-20$ , (f,l) day 0. 44
- 10 (a) as in figure 7(b) but rotated by  $90^\circ$ . (b) Hovmöller diagram of OLR anomalies ( $\text{W m}^{-2}$ ; shaded, see legend) averaged over  $15^\circ\text{N}\text{--}15^\circ\text{S}$  for the period from 150 days prior to until 30 days after the primary event on 24 September 2004. 45

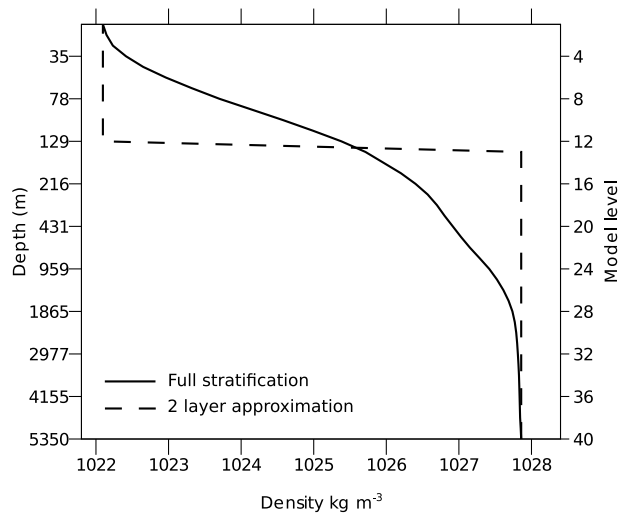


FIG. 1. Potential density profiles used as the model initial conditions. Solid line: default 40 level density profile, calculated from Levitus et al. (2002); Dashed line: two-layer density configuration.

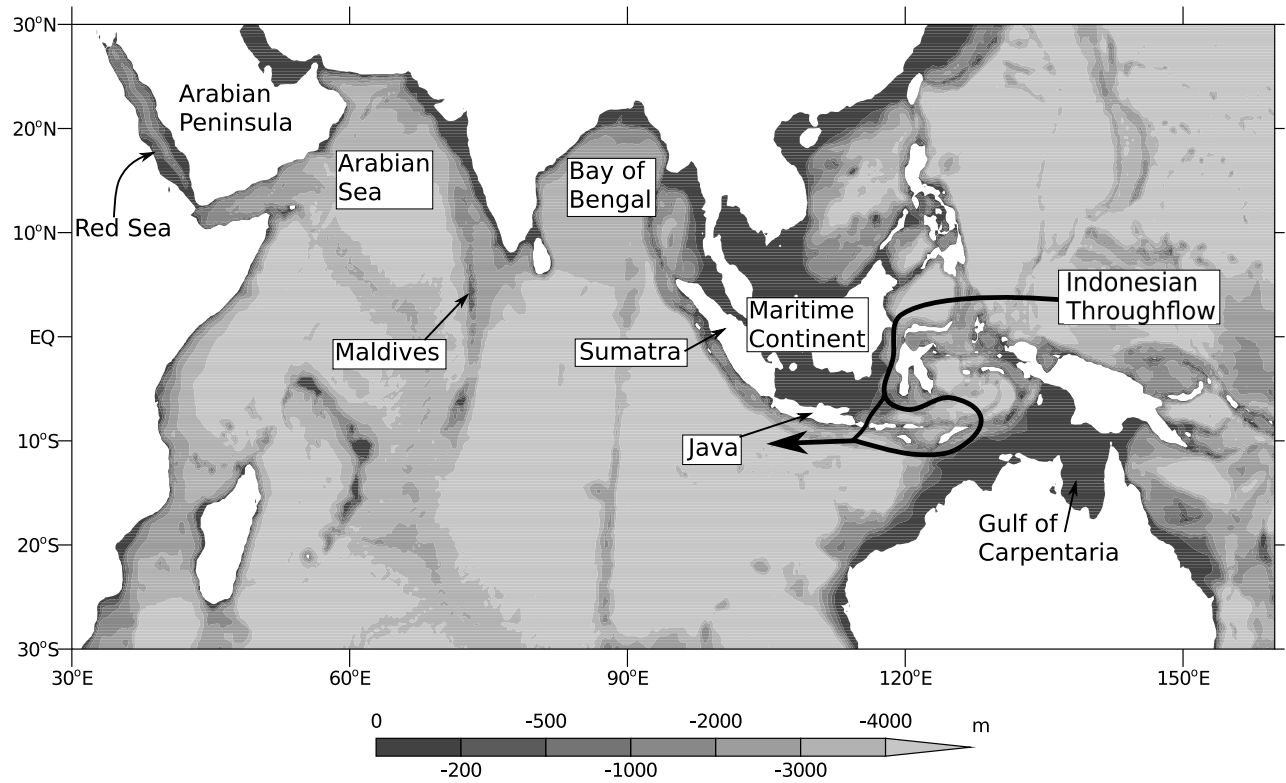


FIG. 2. Model bathymetry at  $1/3^\circ$  resolution (depth shaded in m; see legend). Labels refer to regions mentioned in this study.

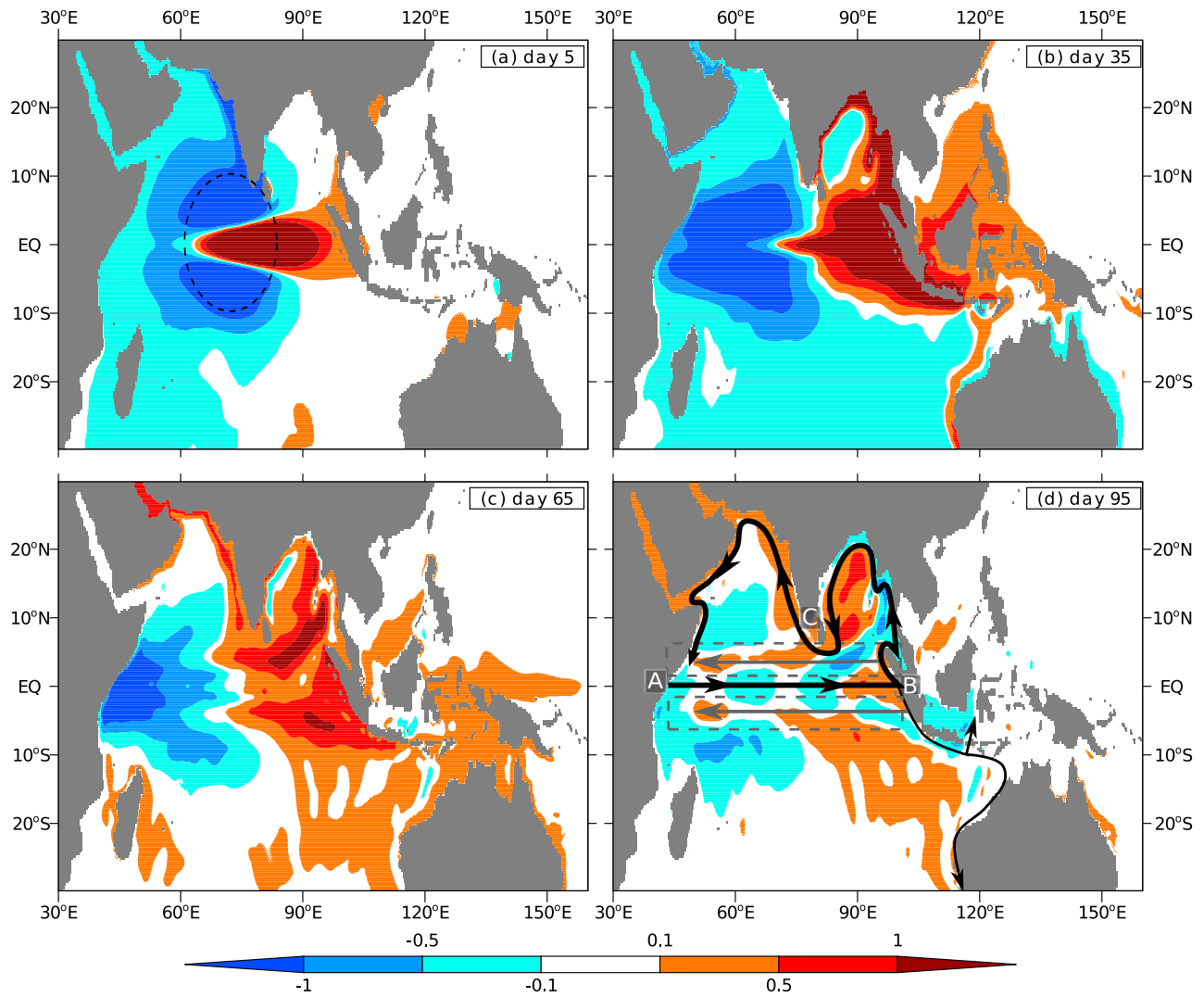


FIG. 3. SSH anomalies (cm) from the control run of the idealised westerly wind burst experiment. (a) day 5, (b) day 35, (c) day 65, (d) day 95. The equatorial wind patch forcing is indicated schematically by the dashed ellipse in (a). In (d), the equatorial and northern coastal Kelvin-waveguide is shown by the thick black line, the southern coastal waveguides by thin black lines and the equatorial Rossby waveguide by the grey arrows and dashed boxes.

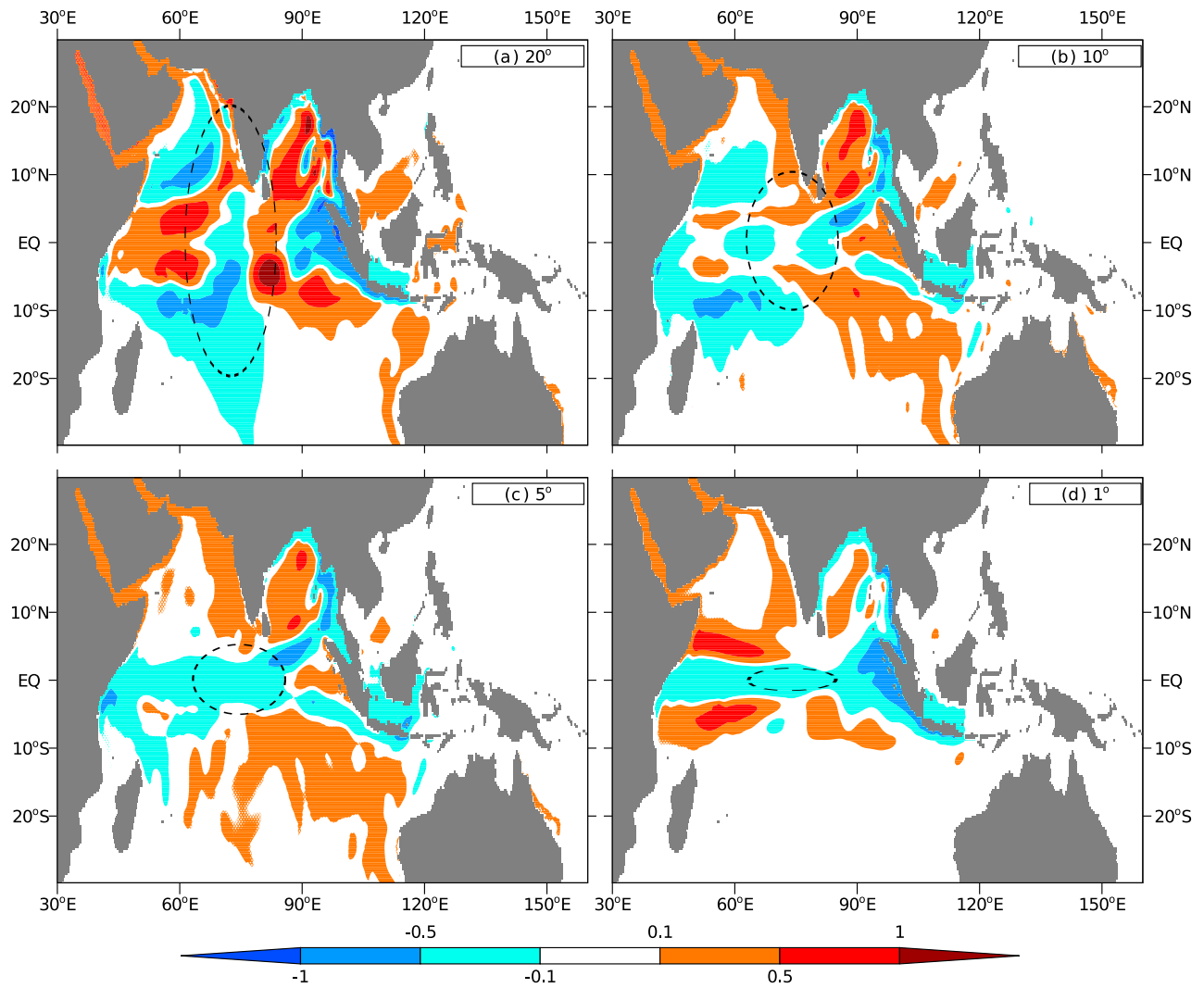


FIG. 4. SSH anomalies (cm) at day 95 for idealised westerly wind burst integrations with differing latitudinal decay scales of the initial wind patch forcing, shown schematically by the dashed ellipses. (a)  $20^\circ$ , (b) control run;  $10^\circ$ , (c)  $5^\circ$ , (d)  $1^\circ$ .

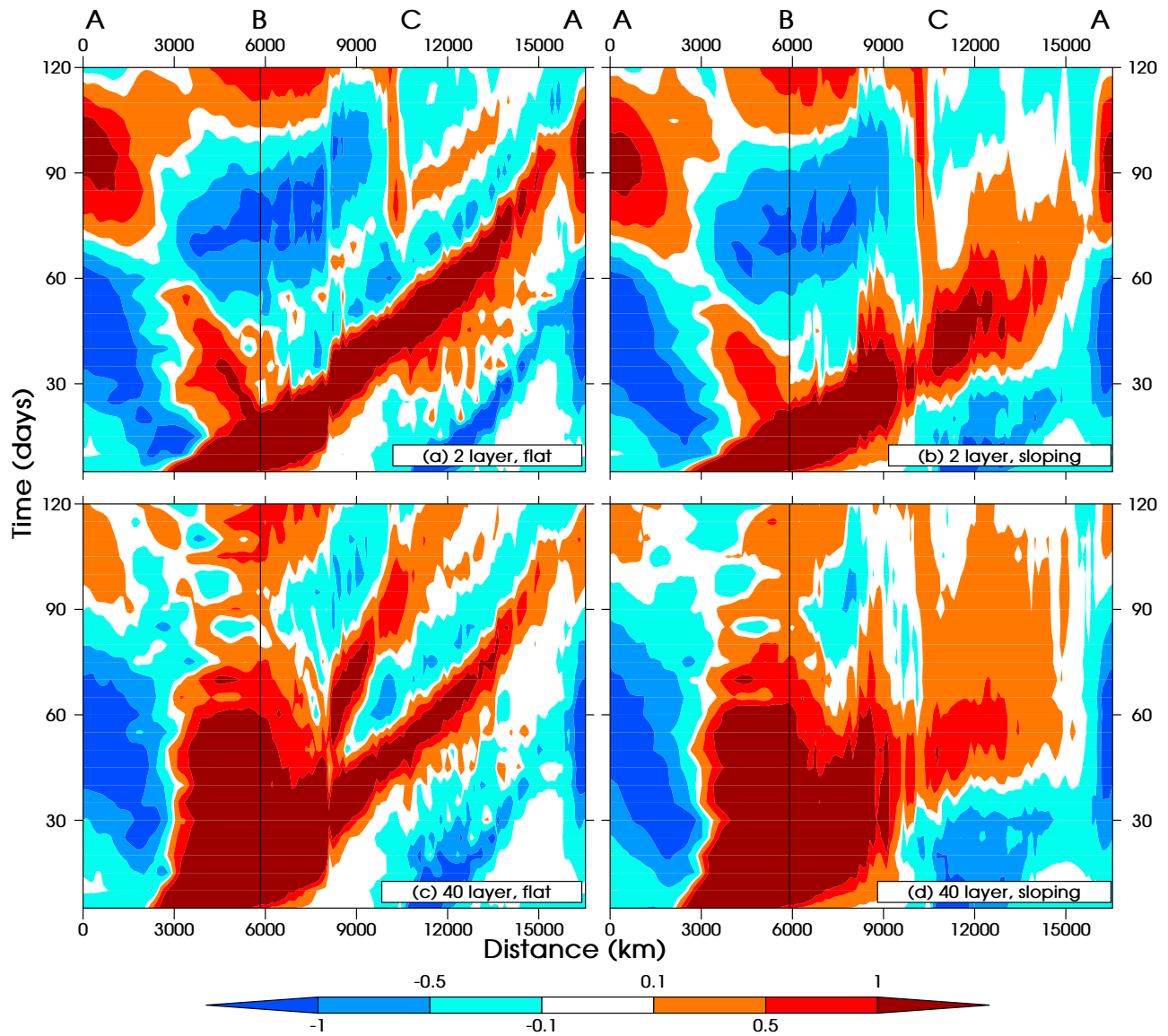


FIG. 5. Hovmöller diagrams of SSH (cm) along the equatorial and coastal Kelvin-waveguides, as shown by the thick black line in Figure 3(d). (a) 2-layer model with flat bathymetry, (b) 2-layer model with sloping bathymetry, (c) full stratification but flat bathymetry, (d) full model with sloping bathymetry. The transition between the equatorial and coastal waveguides is at 5800km, as shown by the black vertical lines. The letters A, B, C along the top axes correspond to the locations marked in Figure 3(d).

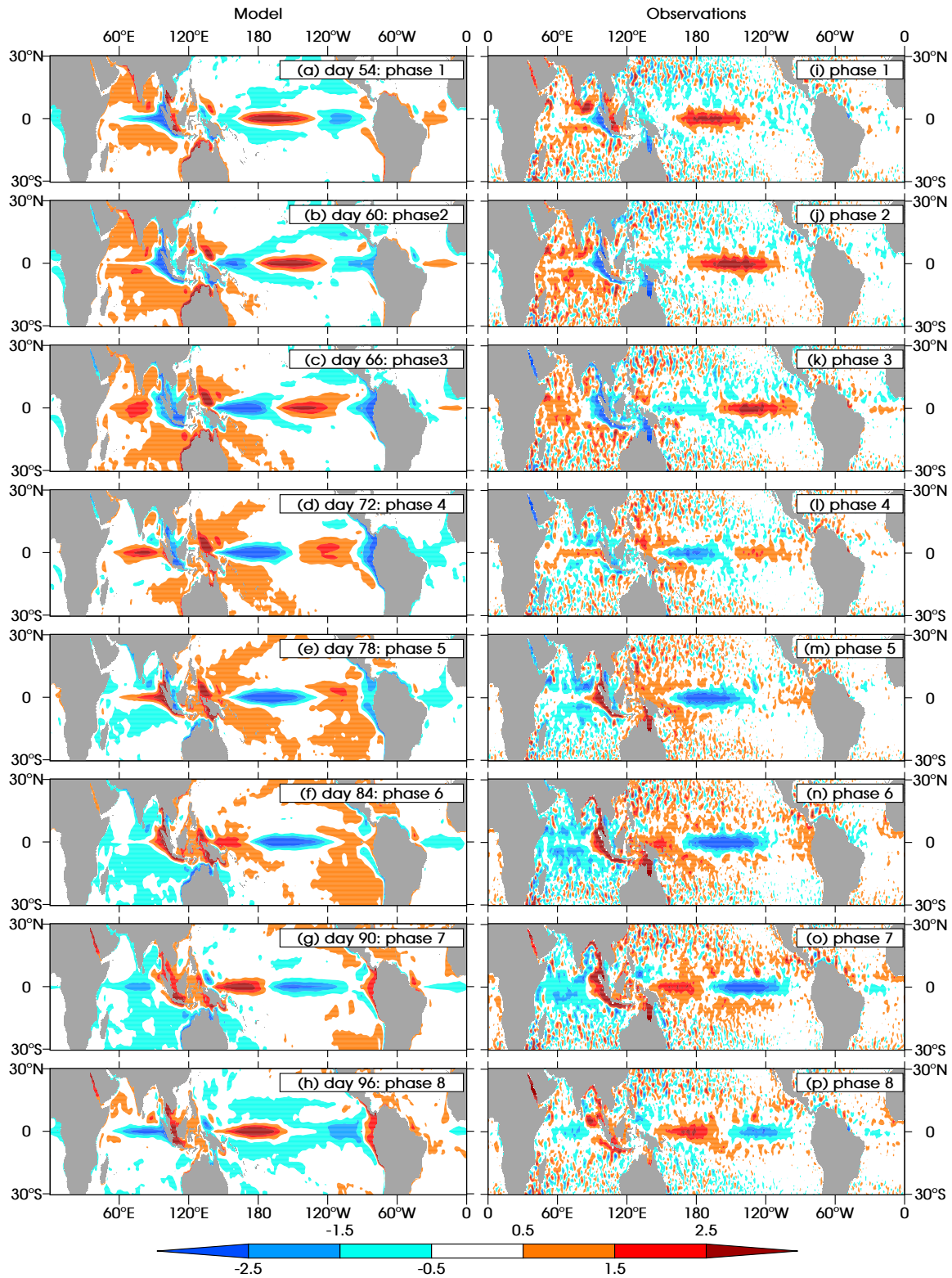


FIG. 6. SSH anomalies (cm) (a–h) from the model run with cyclical composite surface wind forcing, taken from days 54–96, corresponding to a full MJO cycle. (i–p) Composite SSH anomalies (cm) from satellite altimetry observations for the equivalent MJO phases.

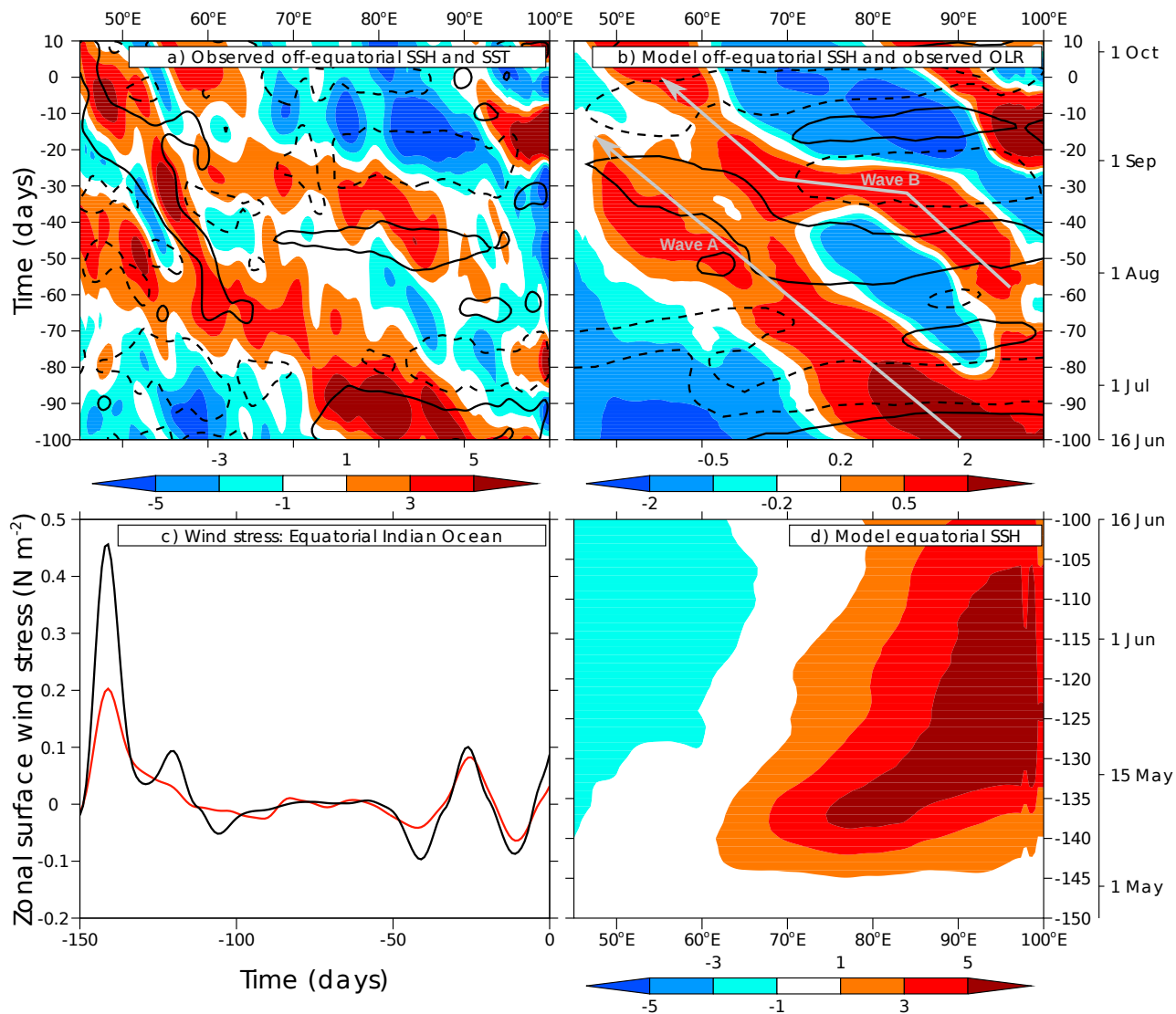


FIG. 7. (a) Hovmöller diagram of observed off-equatorial SSH (cm; shaded, see legend) and SST anomalies (contoured at  $\pm 0.3^\circ\text{C}$ , negative contour dashed) averaged over  $2\text{--}5^\circ\text{N}$  and  $2\text{--}5^\circ\text{S}$  for the 100 days preceding the primary event of 24 September 2004. (b) Hovmöller diagram of off-equatorial SSH from the model run forced by observed winds for the 150 days preceding the primary MJ event and observed equatorial ( $5^\circ\text{S}\text{--}5^\circ\text{N}$ ) OLR anomalies (contoured at  $\pm 15 \text{ W m}^{-2}$ , negative contour dashed) from day  $-100$  to  $+10$ . (c) Surface zonal wind stress anomalies ( $\text{N m}^{-2}$ ) averaged over  $10^\circ\text{N}\text{--}10^\circ\text{S}$  and:  $40\text{--}100^\circ\text{E}$  (red line);  $70\text{--}80^\circ\text{E}$  (black line). (d) Hovmöller diagram of equatorial ( $2^\circ\text{N}\text{--}2^\circ\text{S}$ ) SSH from the same model run as (b) but for days  $-150$  to  $-100$ .

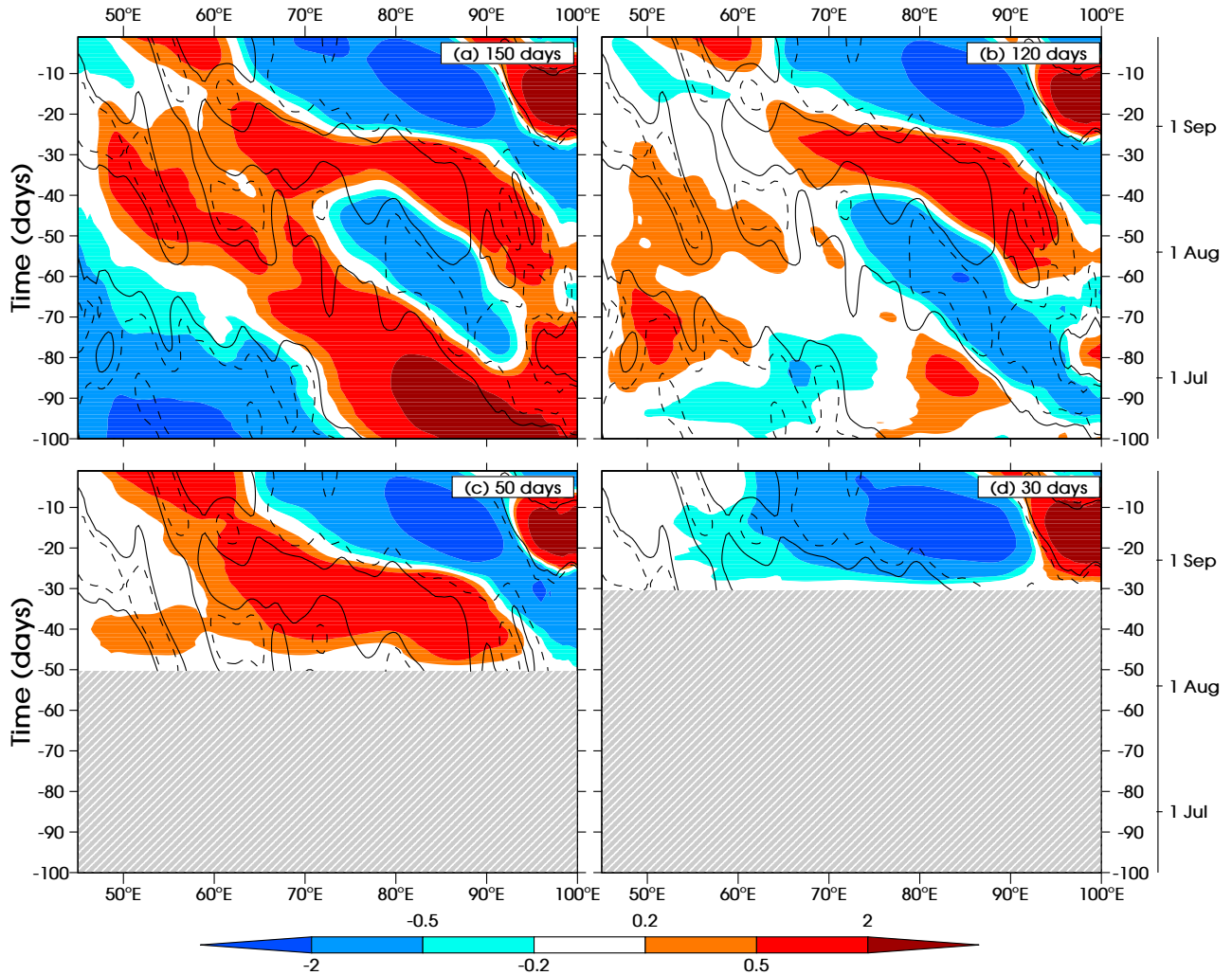


FIG. 8. Hovmöller diagrams of model SSH (cm; shaded, see legend) and observed SSH anomalies (contoured at  $\pm 1$  cm, negative contour dashed) for the 100 days preceding the primary event on 24 September 2004. The model integrations were forced with observed wind stress, and started at (a) 150 days, (b) 120 days, (c) 50 days, (d) 30 days prior to the start of the primary MJ event on 24 September 2004 (day 0).

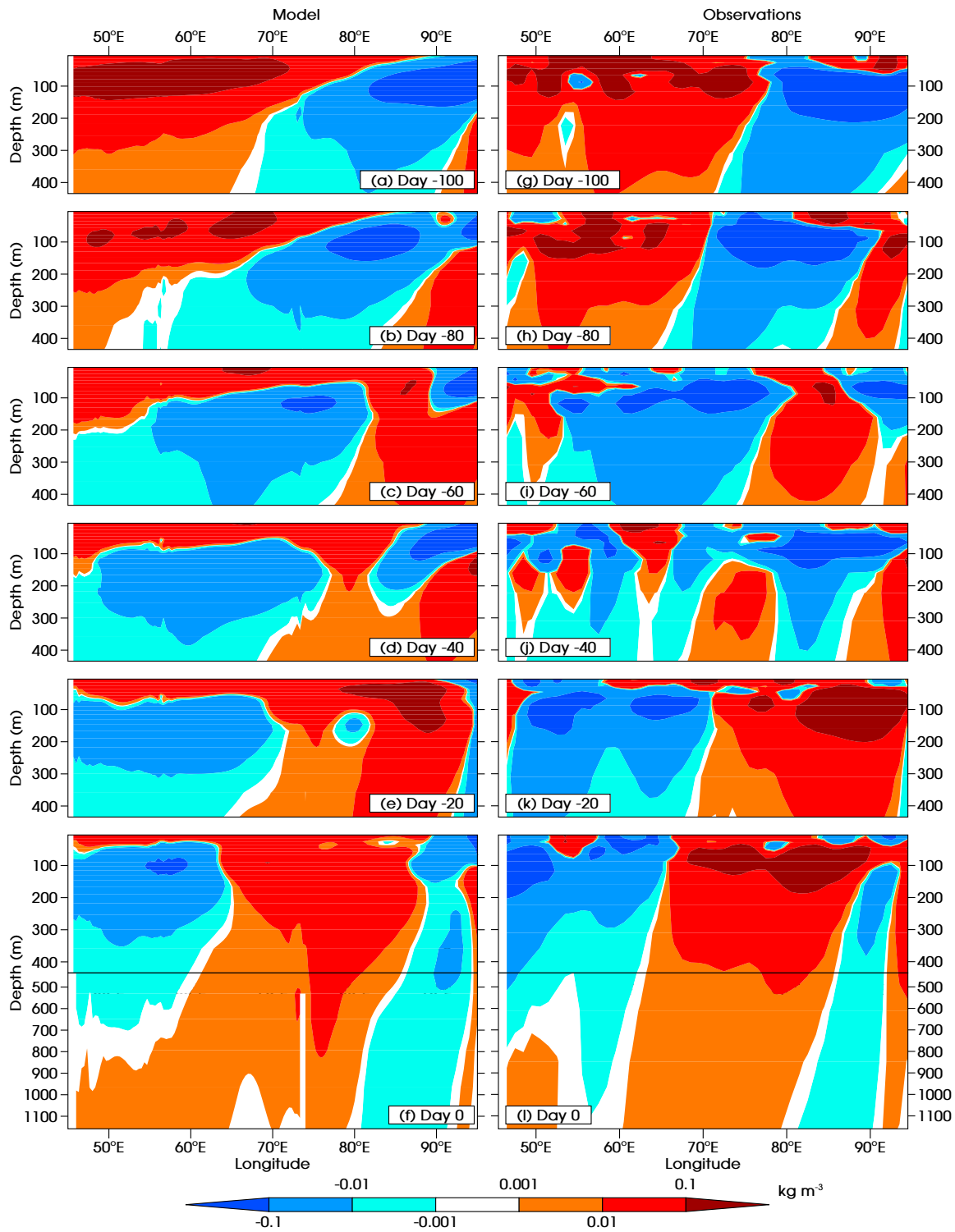


FIG. 9. Vertical profiles of density anomalies ( $\text{kg m}^{-3}$ ; shaded, see legend) for the 100 days preceding the primary event on 24 September 2004 in: (a–f) the model simulation forced by observed winds over the 150 days prior to the primary event; (g–l) “observations” from the ECCO-GODAE ocean state estimation. (a,g) day –100, (b,h) day –80, (c,i) day –60, (d,j) day –40, (e,k) day –20, (f,l) day 0.

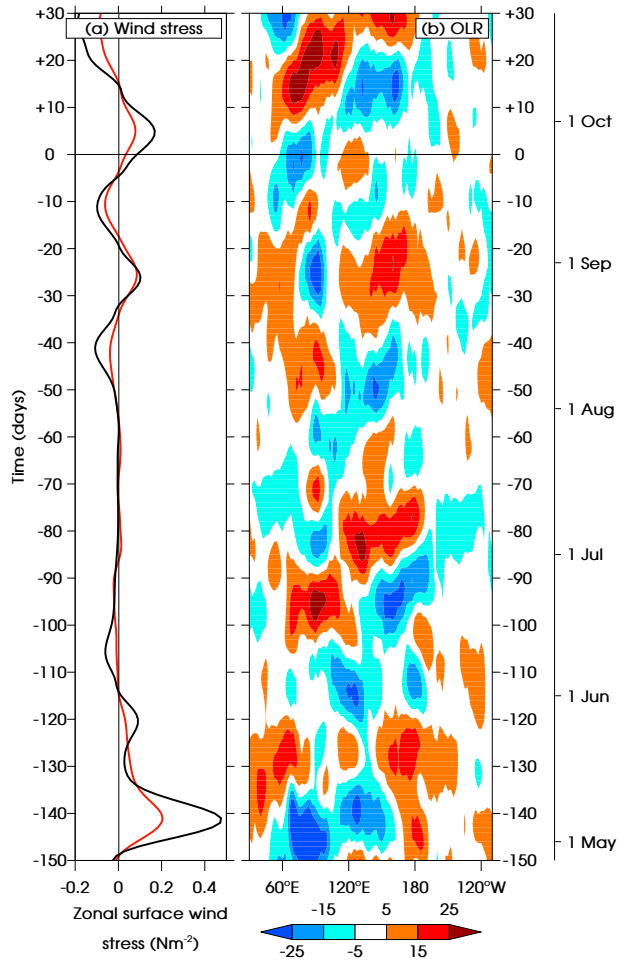


FIG. 10. (a) as in figure 7(b) but rotated by  $90^\circ$ . (b) Hovmöller diagram of OLR anomalies ( $\text{W m}^{-2}$ ; shaded, see legend) averaged over  $15^\circ\text{N}$ – $15^\circ\text{S}$  for the period from 150 days prior to until 30 days after the primary event on 24 September 2004.